1 The PAMELA apparatus.

The PAMELA apparatus is inserted inside a pressurized container (2 mm aluminum window) attached to the Russian Resurs-DK1 satellite. The apparatus, approximately 130 cm tall and with a mass of about 470 kg, can be seen in Figure s1, which shows a 68 GeV positively-charged particle selected as a positron. It comprises the following detector systems (from top to bottom): a time-of-flight system (ToF (S1, S2, S3)); a magnetic spectrometer; an anticoincidence system (AC (CARD, CAT, CAS)); an electromagnetic imaging calorimeter; a shower tail catcher scintillator (S4) and a neutron detector. The ToF system provides a fast signal for triggering the data acquisition and measures the time-of-flight and ionization energy losses (dE/dx) of traversing particles. It also allows down-going particles to be reliably identified. Multiple tracks, produced in interactions above the spectrometer, were rejected by requiring that only one

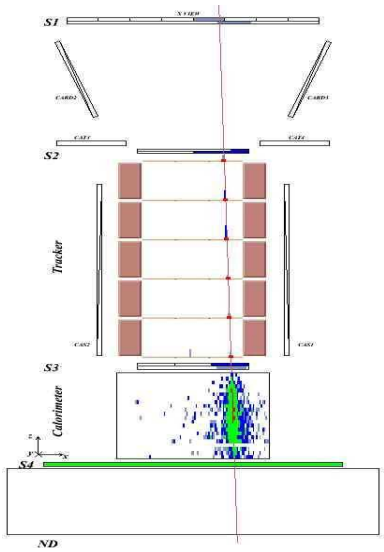

Figure s1. A 68 GeV positively-charged particle selected as positron. The bending (x) view is shown. The signals as detected by PAMELA detectors are shown along with the particle trajectory (solid line) reconstructed by the fitting procedure of the tracking system. The calorimeter shows the typical signature of an electromagnetic shower (plane 19 of the calorimeter x-view was malfunctioning).

strip of the top ToF scintillator (S1 and S2) layers registered an energy deposition ('hit'). Similarly no hits were permitted in either top scintillators of the AC system (CARD and CAT). The central part of the PAMELA apparatus is a magnetic spectrometer consisting of a 0.43 T permanent magnet and a silicon microstrip tracking system. The spectrometer measures the rigidity of charged particles through their deflection in the magnetic field. During flight the spa-

tial resolution is observed to be 3μm corresponding to a maximum detectable rigidity (MDR) exceeding 1 TV. The dE/dx losses measured in S1 and the silicon layers of the magnetic spectrometer were used to select minimum ionizing singly charged particles (mip) by requiring the measured dE/dx to be less than twice that expected from a mip. The sampling calorimeter comprises 44 silicon sensor planes interleaved with 22 plates of tungsten absorber. Each tungsten layer has a thickness of 0.26 cm corresponding to 0.74 radiation lengths. Positrons (electrons) can be selected from a background of protons (antiprotons) by studying the properties of the energy deposition and interaction topology. A high dynamic-range scintillator system and a neutron detector are mounted under the calorimeter at the bottom of the apparatus.

2 Electron and positron identification

Electrons and positrons can be reliably distinguished from the other cosmic-ray species impinging on PAMELA (mostly protons) by combining information provided by the different detector components. A permanent magnet spectrometer with a silicon tracking system allows the rigidity and sign-of-charge of the incident particle to be determined. The interaction pattern in a imaging silicon-tungsten calorimeter allows electrons and positrons to be separated from protons.

The misidentification of electrons and, in particular, protons is the largest source of background when estimating the positron fraction. This can occur if the sign-of-charge is incorrectly assigned from the spectrometer data, or if electron- and proton-like interaction patterns are confused in the calorimeter data. Due to the finite spatial resolution in the spectrometer, high rigidity (low deflection) electrons may 'spill over' into the positron sample (and vice-versa) if assigned the wrong sign-of-curvature. This spillover background was eliminated by imposing a set of strict selection criteria on the quality of the fitted tracks. The spillover limit for positrons is estimated from flight data and simulation to be approximately 300 GeV, as expected from particle beam tests. The antiproton-to-electron flux ratio in the cosmic radiation is approximately 10^{-2} between 1 and 100 GV but can be reduced to a negligible level after electrons are selected using calorimeter information. However, as described in the main text, the proton background vastly dominate the positron signal. Robust positron identification is therefore required, and the residual proton background must be estimated accurately. The combination of the imaging calorimeter and magnetic spectrometer can provide the proton rejection factor necessary for a clean positron identification. Using particle beam data collected at CERN we have previously shown[31] that less than one proton out of 100,000 passes the calorimeter electron selection up to 200 GeV/c, with a corresponding electron selection efficiency of 80%. However, in this analysis we used a different approach: we tuned the calorimeter identification to select $> 95\%$ of the electrons or positrons and reject 99.9% of the protons and, then, we statistically estimated the residual proton background.

This approach was based on the event characterisation of Figure 1 (main text), i.e. electrons and positrons have an energy fraction variable,$\mathcal{F}$, lying mostly between 0.4 and 0.7 while protons are much more spread out and mostly at $\mathcal{F} < 0.4$. The validity of such event characterisations was confirmed using the neutron yield from the calorimeter and the ionization (dE/dx) losses measured in the spectrometer. These distributions were studied for positively- and negatively-charged events after the calorimeter selection and compared to

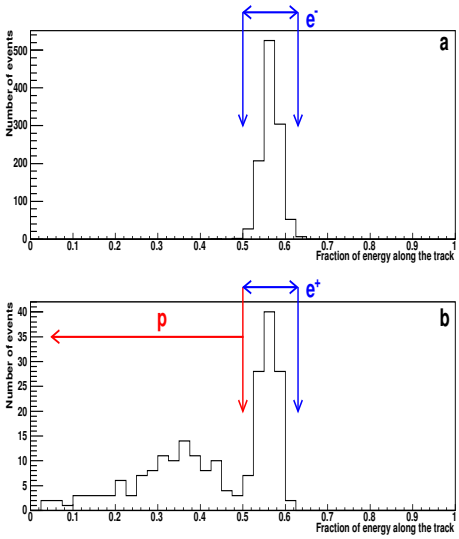

Figure s2. Panels **a** and **b** show the distribution of the energy fraction for negatively and positively charged particles, respectively, selected as in Figure 1 main text. The blue and red arrows indicate the distribution regions dominated by electrons/positrons and protons, respectively.

the corresponding distributions derived from the entire set of data for negatively charged (mostly electrons) and positively charged (overwhelmingly proton) events. A higher neutron yield is expected in hadronic interactions in the calorimeter, especially at energies greater than 10 GeV. Figure s2 shows the distribution of $\mathcal{F}$, for negatively (Panel **a**) and positively (Panel **b**) charged particles in the rigidity range 20-28 GV. Defining e^-, e^+ and p as shown in Figure s2 the corresponding neutron yield can be obtained. This is shown in Figure s3a for e^- and Figure s3b for e^+ (blue histogram) and protons (red histogram). The neutron distribution for positrons appears statistically different from the proton one and similar to the electron one. Indeed, the small difference between the e^- and e^+ distribution can be associated to a residual proton contamination as expected from Figure s2b.

Similarly, competing density and logarithmic rise effects for dE/dx losses in the silicon detectors of the spectrometer yield different dE/dx distributions for electrons and protons between 10 and 25 GeV. This can be seen in Figure

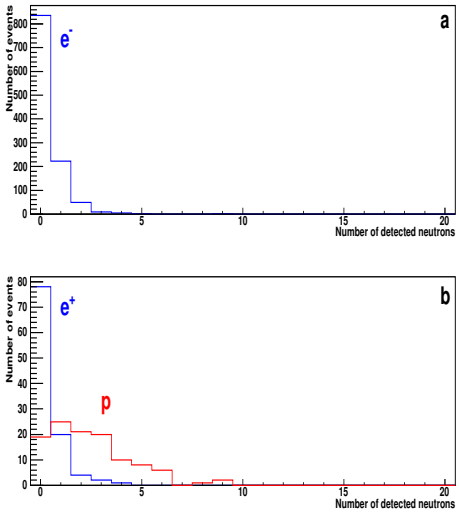

Figure s3. Panels **a** and **b** show the neutron yield for negatively and positively charged particles, respectively, selected according to Figure s2 in the rigidity region 20-28 GV. Blue histograms for e^- and e^+ and red histogram for protons.

s4 that shows these distributions for positively (red histogram) and negatively (blue histogram) charged particles (Panel **a**) and for protons (red histogram) and positrons (blue histogram) (Panel **b**) selected between 15 and 20 GV similarly to Figure s2b. A Kolmogorov-Smirnov test showed that the distributions for events characterised as positrons (protons) were statistically compatible at 95% confidence level with the corresponding negatively- (positively-) charged distributions. This is a particularly important check, as the spectrometer information is independent of the calorimeter and can be used to rule out proton interactions resulting in (e.g.) π^0 production in the topmost calorimeter planes. The π^0 will decay to two photons that can generate electromagnetic showers in the calorimeter.

The event selection methodology was further validated using particle beam data collected prior to launch[31] and data generated using the PAMELA Collaboration's official simulation program. This simulation is based on the GEANT package[32] version 3.21 and reproduces the entire PAMELA apparatus, including the spectrometer magnetic field and the pressure vessel. Similar conclusions were derived from cosmic-ray data collected by the CAPRICE98 balloon-borne experiment[33]. This apparatus was equipped with a similar but thinner (7 radiation lengths) silicon-tungsten calorimeter. A gas-RICH detector allowed background-free samples of protons (i.e. no positron contamination) to be selected up to 50 GeV. Within the limits of available statistics, the reconstructed proton and electron/positron lateral energy distributions were fully consistent with those obtained with the PAMELA calorimeter.

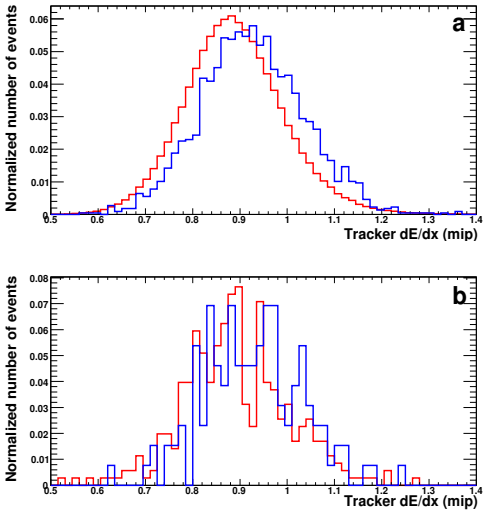

Figure s4. The normalized spectrometer dE/dx distributions for negatively (blue histogram) and positively (red histogram) charged particles (Panel **a**) and for positrons (blue histogram) and for protons (red histogram) (panel **b**) selected between 15 and 20 GV similarly to Figure s2b.

3 Background estimation

While the distribution shown in Figure 1 (main text) presents a clear positron signature, the residual proton background distribution must be quantified. This distribution was obtained using the flight calorimeter data. There was no dependence on simulations. The total calorimeter depth of 22 detector planes was divided in two non-mutually exclusive parts: an upper part comprising planes 1-20, and a lower part comprising planes 3-22. Calorimeter variables (e.g. total detected energy, and lateral shower spread) were evaluated for both parts. Electrons and positrons can be identified in the upper part of the calorimeter using the total detected energy and the starting point of the shower. A nearly pure sample of protons can be obtained in the lower part of the calorimeter (planes 3-22) selecting particles that do not interact in the first 2 planes (only 2% of electrons and positrons with rigidities greater than 1.5 GV pass this condition). The procedure was validated using simulations.

As an example Figures s5a and s6a shows the energy fraction variable, $\mathcal{F}$, for negatively charged particles in the rigidity range 20-28 GV and 28-42 GV, respectively, selected as electrons in the upper half of the calorimeter. Panels (b) and (c) show the $\mathcal{F}$ distributions for positively-charged particles obtained for the lower and upper part of the calorimeter, i.e. protons and protons plus positrons, respectively. The distributions in panels (**a**) and (**b**) are clearly different while panel (**c**) shows a mixture of the two distributions, which strongly

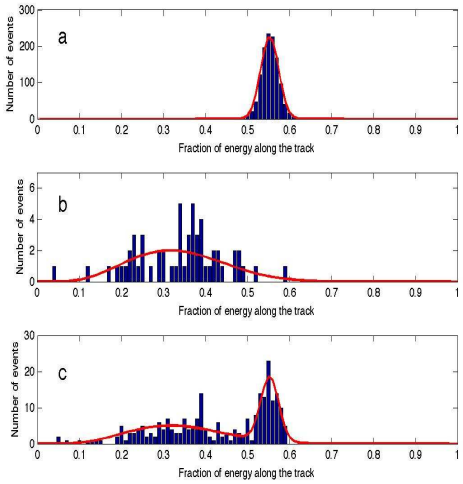

Figure s5. Panel **a** shows the distribution of the energy fraction for negatively charged particles with rigidity between 20 and 28 GV, selected as electrons in the upper part of the calorimeter. Panel **b** shows the same distribution for positively charged particles selected as protons in the bottom part of the calorimeter. Panel **c** shows positively charged particles, selected in the upper part of the calorimeter, i.e. protons and positrons.

supports the positron interpretation for the electron-like $\mathcal{F}$ distribution in the sample of positively charged events. A parametric bootstrap analysis with maximum likelihood fitting was performed on distributions such as those shown in Figures s5 and s6 for a number of rigidity intervals, and the numbers of detected electrons, positrons, and contaminating protons were obtained.

For each energy interval, the distribution of the calorimeter energy fraction ($\mathcal{F}$) for positively-charged particles (e.g. Figure s5c) was expressed as mixture distribution[34] of positrons (i.e. signal, electrons as in Figure s5a) and protons (background, e.g. Figure s5b):

$$f(\mathcal{F}) \;=\; p \cdot g_1(\mathcal{F}; q_1) + (1-p) \cdot g_2(\mathcal{F}; q_2) \qquad (1)$$

where the parameter p gives the mixture proportion; $g_1(\mathcal{F}; q_1)$ and $g_2(\mathcal{F}; q_2)$ are the probability density functions (p.d.f.) for positrons/electrons and protons, respectively. The p.d.f.'s g_1 and g_2 were determined by analysing two samples of pure electrons (e.g. Figure s5a) and protons (e.g. Figure s5b) in the same energy range. We used a Beta distribution for both the electron/positron signal g_1 and for the proton background g_2. In both cases parameter sets q_1 and q_2 were determined from a maximum likelihood fit.

The mixture proportion p was estimated by means of a bootstrap procedure[35] followed by the maximum likelihood method. As first step, the experimental

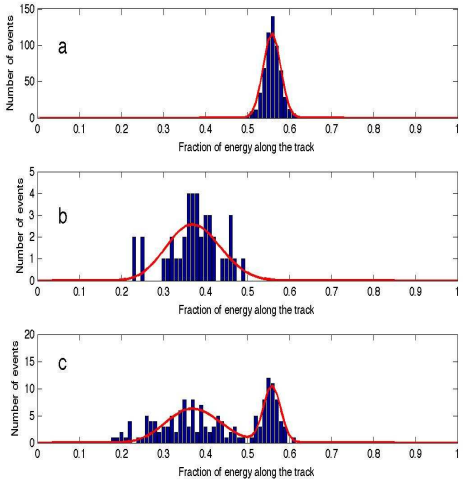

Figure s6. Panel **a** shows the distribution of the energy fraction for negatively charged particles with rigidity between 28 and 42 GV, selected as electrons in the upper part of the calorimeter. Panel **b** shows the same distribution for positively charged particles selected as protons in the bottom part of the calorimeter. Panel **c** shows positively charged particles, selected in the upper part of the calorimeter, i.e. protons and positrons.

distribution was re-sampled, by means of a bootstrap procedure, $N = 1000$ times. For each re-sample i ($i = 1, \ldots N$) we estimated the unknown parameter p_i by means of an un-binned maximum likelihood analysis. The likelihood is defined by:

$$L_i = \Pi_{j=1}^{K}[p_i g_1(\mathcal{F}_j; q_1) + (1 - p_i) g_2(\mathcal{F}_j; q_2)]$$

where K is the total number of positive particles (e.g. Figure 6c).

The best fit point for p_i corresponds to the maximum L_i. Therefore as a result we obtained from eq. 1 N estimations of the number of positrons candidates (n_i^+). Then, the final number of positron candidates was obtained as

$$n = \frac{1}{N} \sum_{i=1}^{N} n_i^+$$

We also estimated the α-level confidence interval including all the values of n_i^+ between the $\alpha/2$ and 1- $\alpha/2$ percentiles of the n_i^+ distribution. We chose one standard deviation as the confidence interval.

An alternative non-parametric statistical method to evaluate the proton background required the construction of a test sample. The test sample was built by combining the proton sample with a weight w and the electron sample

with a weight $1 - w$, with $w \in (0, 1)$. The value of w is chosen by minimizing the Kolmogorov-Smirnov distance between the positive sample and the test one. Furthermore, a Mann–Whitney test is applied around the positron peak in order to check if the two sets are compatible. After the normalization of the test sample, the proton background is found by counting only the proton events (with their own weight) inside the positron selection region. The calculation of the confidence interval is based on the likelihood ratio test[36], by considering proper probability models for the positron signal, the proton background, the selection efficiency and the weight w.

4 Observation of charge-sign dependent solar modulation effects

The solar modulation has a significant effect mostly on cosmic-rays with rigidities less than about 10 GV. This modulation has a time dependence varying from a period of maximum activity and maximum effect on cosmic rays to a minimum in a 11 year time. At each maximum the polarity of the solar magnetic field reverses. Indications that solar modulation effects depend on the cosmic-ray sign-of-charge have been clearly seen in the antiproton-to-proton flux ratio measured before and after the most recent (2000) reversal of the solar magnetic field by a series of flights of the BESS balloon-borne experiment[37]. Then, low energy difference between the PAMELA results and those from CAPRICE94[6], HEAT95[5] and AMS-01[7] (see Figure s7) can be interpreted as a consequence of solar modulation effects. These older results were collected during the previous solar cycle which favored positively-charged particles due to the solar polarity while the current cycle favours negatively-charge particles. Similar effects, but with large statistical uncertainties, were observed by the series of balloon flights of the Aesop positron-electron experiment[10,38] (Figure s7).

In the antiproton case, solar modulation effects were seen mostly at low rigidities (<2 GV), and during a period of maximum solar activity. During the period of solar minimum corresponding to PAMELA data taking, solar modulation becomes negligible in the BESS data-set. In fact the low cosmic-ray antiproton flux limits a detailed study of this effect. In the PAMELA data-set, charge dependent solar modulation effects on electrons and positrons are evident up to nearly 5 GV, even during the current period of minimum solar activity. Contemporary models interpret charge-sign dependent modulation in the heliosphere as being due to various effects such as gradient, curvature and current sheet drift[39]. Drift effects are at their largest during solar minimum conditions and mostly affect low mass particles such as electrons and positrons.

References

[31] Boezio, M. *et al.* The electron-hadron separation performance of the PAMELA electromagnetic calorimeter. Astropart. Phys. **26**, 111-118 (2006).

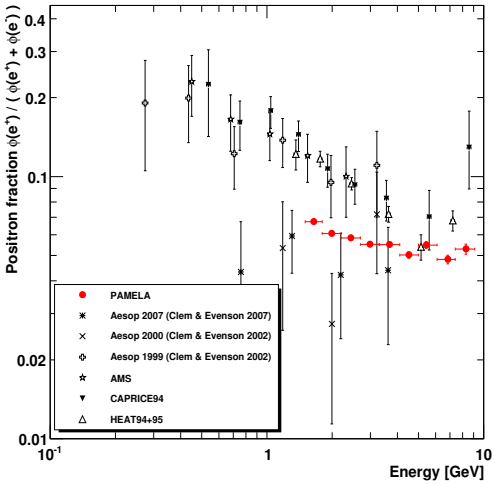

Figure s7. The electron to positron ratio measured by PAMELA, CAPRICE94[6], HEAT95[5], AMS-01[7] and Aesop[10,38]. One standard deviation error bars are shown. If not visible, they lie inside the data points.

[32] Brun, R. *et al.* Detector Description and Simulation Tool, CERN program library (1994).

[33] Boezio, M. *et al.* The cosmic-ray antiproton flux between 3 and 49 GeV. Astrophys. J. **561**, 787-799 (2001)

[34] Everit, B.S. and Hand, D.J. Finite Mixture Distributions. Chapman and Hall (1981).

[35] Efron, B. Bootstrap methods: another look at the jacknife. Ann. Stat. **7**, 1-26 (1979).

[36] Rolke, W. A., Lopez, A. M. & Conrad, J. Limits and confidence intervals in the presence of nuisance parameters. Nucl. Instrum. Meth. A **551**, 493-503 (2005)

[37] Asaoka, Y. *et al.*, Measurements of cosmic-ray low-energy antiproton and proton spectra in a transient period of the solar field reversal. Phys. Rev. Lett. 88, 051101-051104 (2002).

[38] Clem, J. & Evenson, P. Positron abundance in galactic cosmic rays. Astrophys. J. **568**, 216-219 (2002).

[39] Potgieter, M. S., Burger, R. A. & Ferreira, S. E. S. Modulation of cosmic rays in the heliosphere from solar minimum to maximum: a theoretical perspective. Space Sci. Rev. **97**, 295-307 (2001).